Philosophical Magazine

ISSN: 1478-6435 (Print) 1478-6443 (Online) Journal homepage: https://www.tandfonline.com/loi/tphm20

On the glide of [100] dislocation and the origin of 'pencil glide' in Mg_2SiO_4 olivine

S. Mahendran, Ph. Carrez & P. Cordier

To cite this article: S. Mahendran, Ph. Carrez & P. Cordier (2019) On the glide of [100] dislocation and the origin of 'pencil glide' in Mg_2SiO_4 olivine, Philosophical Magazine, 99:22, 2751-2769, DOI: 10.1080/14786435.2019.1638530

To link to this article: https://doi.org/10.1080/14786435.2019.1638530

Published online: 09 Jul 2019.

PHILOSOPHICAL MAGAZINE
2019, VOL. 99, NO. 22, 2751–2769
https://doi.org/10.1080/14786435.2019.1638530

Taylor & Francis
Taylor & Francis Group

On the glide of [100] dislocation and the origin of 'pencil glide' in Mg_2SiO_4 olivine

S. Mahendran, Ph. Carrez and P. Cordier

Univ. lille, CNRS, INRA, ENSCL, UMR8207 UMET - Unité Matériaux et Transformations, Lille, France

ABSTRACT

Olivine with chemical composition $(Mg,Fe)_2SiO_4$ is a silicate which is supposed to strongly constrain the flow of the Earth's upper mantle under thermal convection. Its mechanical properties are thus of primary importance. Slip systems in olivine involve two types of dislocations with [100] and [001] Burgers vectors. In this study, we report atomistic modelling of screw dislocations with [100] Burgers vector and their intrinsic properties. We show that the [100] screw dislocation core exhibits several configurations corresponding to spreading in different planes and different relative stabilities. At low pressure, we identify a clear tendency for core spreading in (010). At higher pressure, relevant for the Earth's mantle, we show that pressure promotes a change in core configuration with spreading into equivalent {021} planes. Based on the systematic investigation of the minimum energy path between the different configurations, we show that the variability of core structures allows complex glide paths which has been described at the macroscopic level as 'pencil glide'. Our results suggest that the pencil glide is more efficient at high pressure.

ARTICLE HISTORY
Received 5 April 2019
Accepted 20 June 2019

KEYWORDS
Atomistic simulations; olivine; dislocation glide; crystal plasticity

1. Introduction

The so-called 'pencil glide' mechanism was first introduced by Taylor and Elam [1] nearly one century ago to describe the diffuse and wavy slip lines observed in deformed single crystal metallic samples. It is nowadays used to refer to the plastic deformation of a crystal for which the slip directions are well defined but in planes which do not necessarily contain the slip direction. In *bcc* metals, the lack of planar slip traces is often though to result from sufficiently frequent cross slip events of screw dislocations which ultimately make the dislocation motion fully three dimensional. Consequently, the physical origin of this specific deformation behaviour is related to the atomic configuration of the

CONTACT Ph. Carrez philippe.carrez@univ-lille.fr Univ. lille, CNRS, INRA, ENSCL, UMR8207 UMET - Unité Matériaux et Transformations, Lille F-59655, France

dislocation core structure, with in particular for bcc metals, the occurrence of a non planar core structure for screw dislocations [2,3].

The pencil glide mechanism has also been reported in olivine $(Mg,Fe)_2SiO_4$ [4]. Olivine is a common silicate, main constituent of the upper mantle of the Earth. Its orthorhombic structure (hereafter described using the *Pbnm* space group) can be described as a slightly distorted *hcp* sub-lattice of oxygen ions with cations occupying part of octahedral and tetrahedral interstitial sites. Deformation experiments performed on single crystals show the occurrence of [100] and [001] slip in olivine [5,6], corresponding to classical $< a >$ and $< c >$ slip of the *hcp* lattice. Transmission electron microscopy examinations of either naturally or experimentally deformed samples in various conditions usually report slip of dislocations with [001] Burgers vector in (010), (100) or (110) at low temperature [7–12]. At high temperature, the [100](010) slip system has been documented but also slip systems [100]{0kl} have been reported leading to invoke pencil glide of dislocations with [100] Burgers vectors. Since the early work of Rayleigh [4], pencil glide mechanism in olivine has been continuously invoked notably for the modelling of Crystal Preferred Orientations (CPOs) which may strongly affect seismic waves travel times and give rise to seismic anisotropy [13].

Despite its importance to understand the nature of thermal convection in the upper mantle of the Earth, theoretical modelling of olivine strength and plastic properties remains rather scarce. Peierls-Nabarro (PN) models of dislocation core structures in olivine have been proposed by Durinck and co-workers, based on *ab initio* computation of generalised stacking fault (GSF) energies [14]. However, some primary attempts to model dislocation core structures in olivine based on the full atomistic description [15] demonstrated that in case of a complex crystal structure, the use of a semi-continuum model may suffer from strong intrinsic limitations (such as the assumption of planar core configurations). Moreover, due to the importance of olivine to our understanding of convection in the upper mantle, the effect of high pressure on the dislocation core structures, the slip systems and the strength of olivine cannot be neglected. For instance, the competition between [100] and [001] slip have been proposed to explain the reduction of seismic anisotropy observed at a depth greater than 200 km [16]. However, there is no consensus and the interpretation of this seismic observation is still a matter of debate which includes the effect of pressure on the slip systems activity or the influence of chemistry with the incorporation of dissolved hydroxyl species [17].

In this work, we investigate the dislocation core properties of dislocation with [100] Burgers vector in forsterite Mg_2SiO_4, the magnesium-rich end-member of olivine. As the selection of glide plane can be governed by subtle atomic effects in the core of screw dislocations [18], we focus on the screw core dislocation properties and their associated energy landscapes. To contribute to the debate on the effect of pressure on dislocation properties in olivine, calculations have been

performed in a pressure range 0–10 GPa spanning over the natural Earth upper mantle conditions. The numerical simulation setups and methods are described in the following section. The results obtained are detailed in the results section subdivided into low-pressure and high-pressure behaviours. Finally, our findings are discussed in relation with the current state of the art.

2. Methods

Forsterite Mg_2SiO_4 is modelled using the so-called THB1 semi-empirical potential [19–21]. This potential model is based on an ionic pair potential description using formal charges combined with classical Buckingham form at short range, supplemented by a harmonic three-body term to represent the directionality of O-Si-O bonds of SiO_4 tetrahedra [22] and a shell model [23] to account for oxygen polarizability. The parameterisation of the force field have been successfully used for modelling bulk, defect properties of forsterite [20,24–28] and also olivine phase transformations [29,30] emphasising the transferability of the parameterisation to high pressure calculations. In this work, all the simulations have been performed using the LAMMPS molecular simulation package [31] for which THB1 has been recently implemented as a potential library [27].

Throughout this study, the simulations have been performed using a periodic system containing a single straight infinite dislocation (Figure 1). The system reference vectors (*x, y, z*) are aligned with the crystallographic directions of the forsterite structure, i.e. (*x,y,z*)⇔([100],[010],[001]). Two different system configurations have been considered so that the periodicity in (010) or (001) crystallographic planes are satisfied once a dislocation line of Burgers vector b is inserted. As the dislocation line is along the *x* direction, a component ***b***/2 is

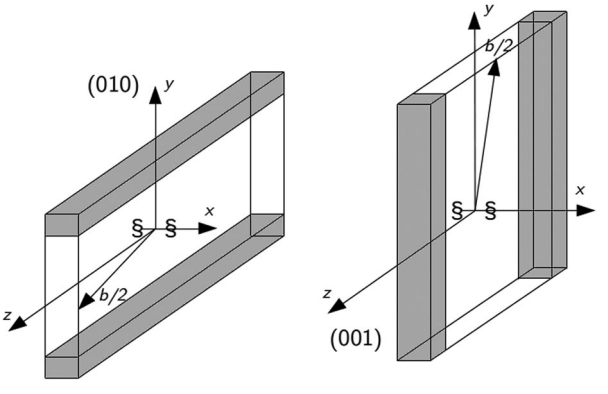

Figure 1. Schematics of the semi-periodic systems. The *x* direction is aligned with the [100] dislocation line direction and the system length along *x* is taken equal to the length of the Burgers vector **b**. The directions *y* and *z* are parallel to [010] and [001] respectively. The systems are made periodic in (010) or (001) by adding a b/2 component to the *z* axis or *y* axis. Regions of fixed ions positions (in grey) are used to avoid any spurious effects due to periodic boundary conditions.

added to either the y or z vector so that the boundaries of periodic replicas match along (001) or (010) respectively. Then, a shield is applied along respectively the z or y direction by considering an inside region where full atomic degrees of freedom are allowed and an outer one where atoms are maintained fixed at their positions resulting from the application of a [100] screw dislocation elastic displacement field. For both as-built configurations, finite size effects were taken into account by increasing the representative volume dimensions to systems containing 22400–44800 ions. The Nudged Elastic Band (NEB) method [32] as implemented in LAMMPS is used to investigate the energy landscape surrounding the dislocation through the computation of the minimum energy path (MEP) between two positions of the defect. The energy profile is sampled using up to 23 images and a spring constant of 0.1 eV/Å. As NEB calculations involve the use of damped dynamics energy minimisation, the simulations are performed using adiabatic dynamics [33], i.e. allocating to each shell a fraction of mass of its corresponding core (a shell mass fraction of 10% ensures maximal numerical stability during the simulations) and integrating the motions in the same way as that of the core, by integration of classical equations of motion with a time step of 0.1 fs. Such a method has been applied to various ionic materials and has been proved successful and computationally efficient [33–36]. As built, the two simulation cells can also be used to investigate the dislocation behaviour under σ_{xy} or σ_{xz} stress loading. This is achieved by applying a simple shear strain component (ε_{xy} or ε_{xz}) to the simulated volume. Depending on the reference frame, such applied stress conditions correspond to a maximum resolved shear stress for glide in (010) or (001).

3. Results

3.1. Screw dislocation core configurations

In the forsterite Mg_2SiO_4 structure, we identified three different [100] screw dislocation core configurations which according to the magnitude of applied pressure, are found to be stable, metastable or unstable. A systematic investigation of these core structures reveals that the dislocation core is systematically centred on one of two typical sites labelled [A] and [B] as depicted in Figure 2. These dislocation centre sites are equally spaced in the structure and located in between cations sites of the crystallographic (010), (001) or {011} planes (corresponding of prism type planes of the *hcp* anions lattice) as shown Figure 2. Thus, [A] sites are surrounded by [B] sites and vice versa.

For a dislocation centred in [A] site, the screw dislocation with [100] Burgers vector is found to be spread in (010) only (Figure 3a). Although the analysis of the atomic disregistry across (010) reveals a tendency for planar core spreading, the two fractional dislocations strongly overlap and lead to a rather compact core configurations. In the following, we refer to this configuration as *compact (010)*

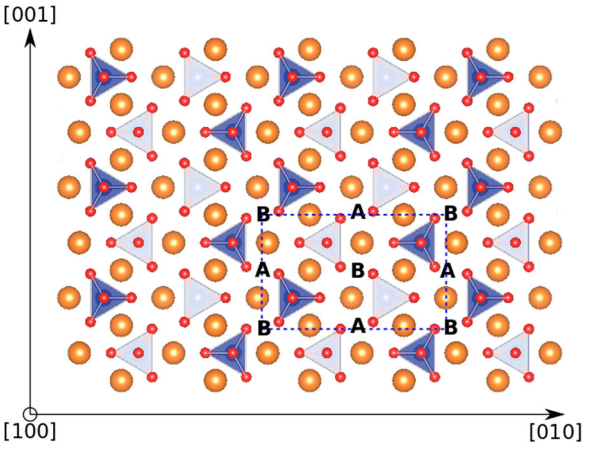

Figure 2. Forsterite Mg_2SiO_4 crystal structure viewed along [100]. Si atoms are at the centre of tetrahedra delimited by the red atoms displaying the oxygen positions. The Mg cations are shown as gold atoms. The sites, labelled [A] and [B], correspond to some specific positions for the screw dislocation core. As these two sites are symmetrically related, their respective roles are reversed if one considers a screw dislocation of opposite Burgers vector.

core. The two others configurations are observed in case of a dislocation centred in [B] site. A first one corresponds to a screw dislocation core fully spread in (010) which splits into two partials dislocations of 1/2[100] Burgers vectors (Figure 3b). Whatever the isostatic pressure applied, the two partial dislocations are located close to the adjacent [A] sites in (010) leading to a dissociation width of the order of magnitude of the [001] lattice repeat. This configuration will be referred as *split (010) core*. A second core configuration, as depicted in Figure 3 (c), shows a clear tendency to spread in {021} planes. Due to the *Pbnm* lattice, depending on the [B] site of the lattice, such core configuration has two variants corresponding to either a spreading in (021) or a spreading in $(0\bar{2}1)$ but one can easily check that the two variants have exactly the same core width and the same core energy as shown below. In the following, we will refer to this configuration as *compact {021} core* since through the whole pressure range investigated here, this configuration remains the one shown Figure 3(c) with no evidence of any fractional dissociation. The relative stability of these three core configurations (Table 1) with respect to the applied confining pressure has been determined by computing the energy of a periodic system within a periodic quadrupolar arrangement [37]. Indeed, for screw dislocations, a quadrupolar arrangement minimising the stored elastic energies allows for a precise computation of the energy of the defects [38,39]. Thus, it turns out that at low pressure, below 4 GPa, the configurations spread in (010) are the most favourable. In particular, at 0 GPa, the split (010) core corresponds to the ground state configuration of the screw [100] dislocation and the compact (010) core is metastable as for the compact {021} core. As pressure increases, the dissociation into partial dislocations becomes less favourable and in the range 2–4 GPa, the stable

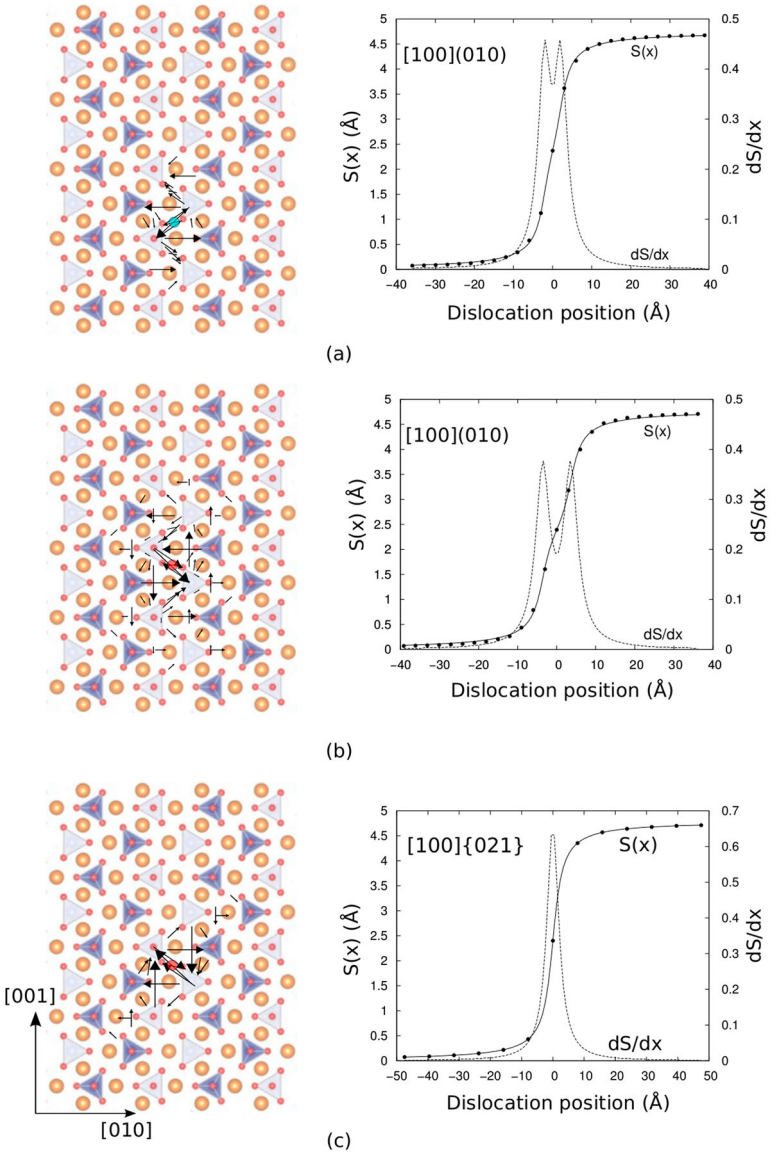

Figure 3. [100] screw dislocation core configurations. For each configuration, the differential displacement map (left panel) is plotted according to Si and O sub-lattices (the anions neighbours list is chosen with respect to the pseudo equivalent *hpc* lattice). Arrows linking neighbours are drawn proportionally to the differential displacement of atoms with respect to the perfect crystal. On the right panel, the corresponding disregistry function *S* in the spreading plane and its derivative is plotted versus the distance *x* to the core centre. (a) Typical compact (010) core centred on a [A] site (computed at 2 GPa). The strong overlapping of the Burgers vector density suggests a compact core spread in (010). (b) Typical split (010) core centred on a [B] site (computed at 0 GPa). The dissociation into two 1/2[100] partial dislocations is revealed by the inflection of the disregistry curve and the well-defined individual peaks of the Burgers vector density *dS/dx*. (c) Typical compact {021} core centred on [B] site (computed at 6 GPa). The differential displacement map reveals the spreading of the core in $(0\bar{2}1)$. Note that a similar configuration can be found in (021).

Table 1. Excess energy (eV/b) of the different core configurations, given with respect to the ground state configuration (indicating by -) at each pressure.

	Core configuration		
Pressure (GPa)	Split (010)	Compact (010)	Compact {021}
0	–	0.31	0.84
2	0.02	–	0.13
4	0.41	0.12	–
6	0.93	0.40	–
8	1.45*	0.59	–
10	1.97*	0.92	–

*Unstable configuration deduced from MEP calculations, see the text for details

configuration of the screw dislocation corresponds to the compact (010) core. At high pressure, above 4 GPa, the ground state configuration of the screw dislocation is the compact {021} core. Thus, the compact (010) core is metastable at high pressure as for the split (010) configuration which becomes unstable above 8 GPa.

3.2. Energy landscape in (010)

In this section, the MEP is first investigated by performing NEB calculations between two equivalent compact (010) core configurations, i.e. between two [A] sites. Figure 4 show the corresponding MEP in (010) plotted using a reaction coordinate linearly interpolated between initial and final states. Along the NEB path, the analysis of the atomic configurations indicates that the dislocation moves along [001] with a core spreading restricted in (010). As the dislocation

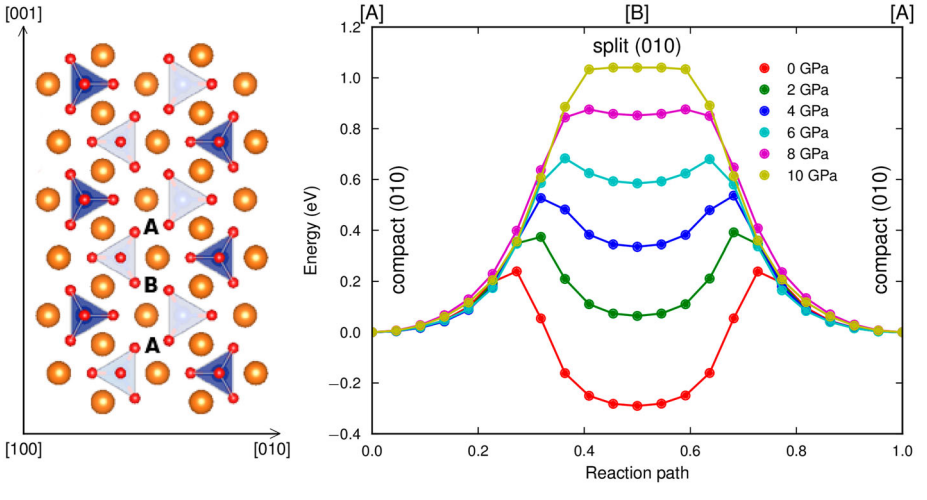

Figure 4. MEP between two consecutive compact (010) core configurations located in [A] type of site and distant from a a [001] lattice repeat. The energies are given for a dislocation line of length b. The analysis of the dislocation core structure along the reaction path reveals that the dislocation moves along a straight path in (010) with at half way, a core centred in [B] corresponding to a split (010) core configuration.

Table 2. Energy barrier (eV/b) associated with the glide in (010).

Pressure (GPa)	Max. energy (eV/b)	σ_c (GPa)
0[a]	0.53 (0.52)	3.2 (3.7)
2	0.37	3.8
4	0.53	4.5
6	0.68	4.9
8	0.87	5.5
10	1.04	5.7

[a]For the 0 GPa calculations, the values reported here correspond to the two MEP shown Figure 5.
Note: The reported critical stress σ_c corresponds to the maximum stress required to overcome the MEP. It is computed according to the derivative of the MEP with respect to the dislocation core position along the path.

core is displaced, the compact (010) core is stretched in (010) with the fractional dislocation densities being more and more separated. As a consequence, at half way of the path, the corresponding dislocation core, centred in a [B] site, exhibits an atomic configuration corresponding to the split (010) core described above. Except for the highest pressure, the MEP show a camel hump shape. As depicted by the negative value of the MEP at half way, the split (010) core configuration is the ground state configurations at 0 GPa (see also Table 1). At higher pressure, this halfway configuration is metastable and ultimately unstable for pressure greater than 8 GPa as mentioned in the previous section.

While the MEP is computed within a semi-periodic system, the relative energy between compact and split (010) configurations are consistent with the ones given in Table 1 resulting from the minimisation of a quadrupolar arrangement of dislocations. Also, it can be noticed that the increase of pressure has an effect on the maximum energy of the MEP which varies from a few tenth of eV/b to one eV/b (Table 2).

Figure 4 shows that at 0 GPa, the MEP is particularly deep and steep around the split (010) core configuration. This suggests that the recombination of the split (010) configuration into the (010) compact core may not correspond to the unique MEP between two consecutive split (010) dislocation configurations. Indeed, a NEB calculation performed at low pressure between two split (010) cores (i.e between two [B] sites) results in a gradual MEP (Figure 5) along which the initial split configuration remains fully dissociated with an intermediate configuration corresponding to a split (010) core with a wider dissociation width. One may yet notice that such widely dissociated core is unfavourable compared to the compact (010) configuration as its excess energy is around 0.4 eV/b (with respect to the 0.3 eV/b of the compact core).

Alternatively, we also investigated the MEP between a compact (010) core and the compact {021} core, *i.e* from a [A] site to a [B] centre position in (010). Figure 6 shows the MEP resulting from a NEB calculation using the two cores as initial and final states in a range 0–10 GPa. Again, the relative core energies are in good agreement with the ones reported in Table 1. Below 4 GPa of pressure, a spreading of the dislocation in (010) is energetically favourable, and the stabilisation of the core spread in {021} is strongly enhanced by the

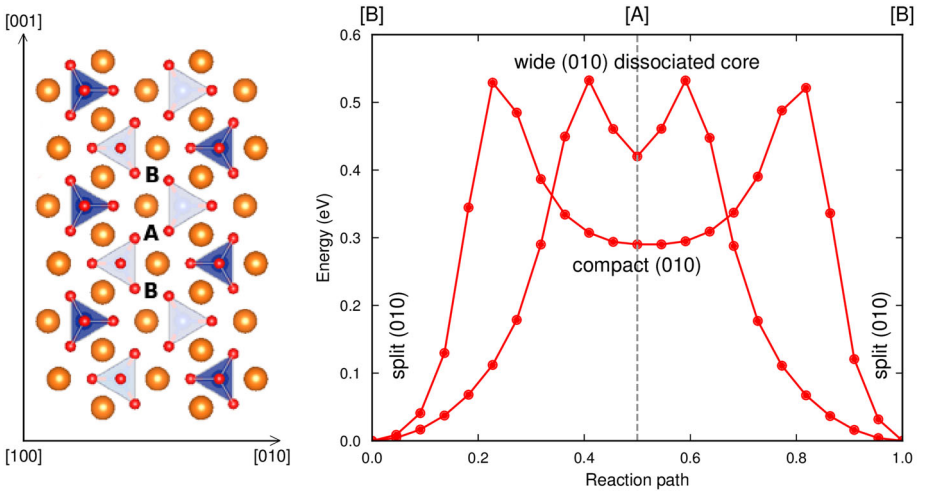

Figure 5. MEP between two consecutive split (010) core configurations located in [B] type of site. The calculation is performed at a pressure of 0 GPa for which the split configuration corresponds to the ground state core configuration. Red circles correspond to the path along which the dislocation evolves through the compact (010) configuration as shown Figure 4. Along the red squares path, the analysis of the atomic configuration indicates that this MEP is achieved by a succession of core state of wider core. At half way, the core is centred in [A] and fully dissociated with a dissociation width between partials 1.5 times larger than the one of the split (010) configuration. One may notice that such a wide dissociation state is of higher energy compared to the compact (010) core.

increase of pressure with a difference of core energy which reaches 0.92 eV/b at 10 GPa of pressure. At all pressures, the transition from one configuration to the other is associated with an energy barrier which increases with increasing

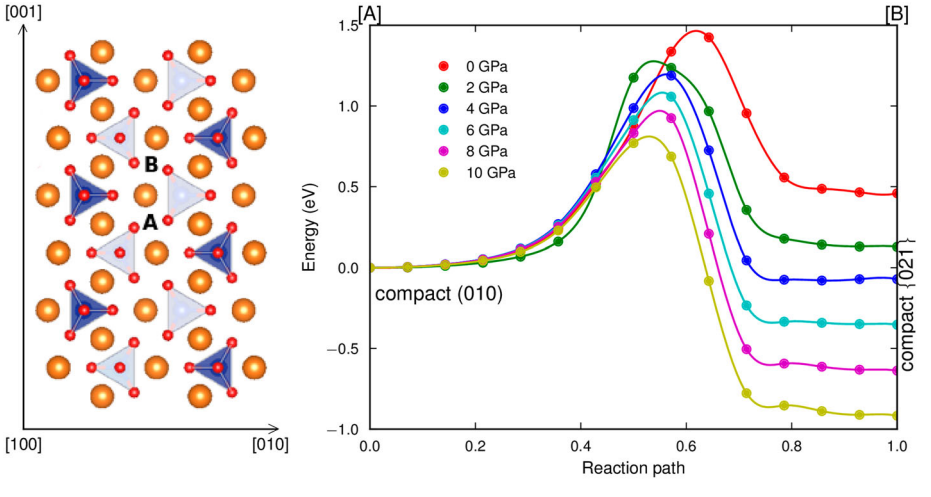

Figure 6. MEP associated with the transition from a compact (010) core to a compact (0$\bar{2}$1) configuration, i.e between [A] and [B] sites in (010). The energies are given for a dislocation line of length b.

Table 3. Energy barrier (eV/b) associated with the transition from a compact (010) core to a compact {021} configuration.

Pressure (GPa)	compact (010) →compact {021}	compact {021} →compact (010)
0	1.42	0.96
2	1.24	1.11
4	1.19	1.26
6	1.06	1.41
8	0.92	1.56
10	0.77	1.69

pressure from 1.24 eV/b to more than 1.69 eV/b (Table 3). Compared to Figure 4, the transition from compact (010) core to compact {021} configuration is thus associated with larger energy barriers throughout the range of pressure investigated here.

3.3. Energy landscape in (0kl)

Above 4 GPa of isostatic pressure, the calculations of dislocation core structures show a strong modification in the ground state dislocation core configurations. The stable core configuration (Table 1), as depicted in Figure 3(c), shows a tendency to spread in {021} planes with a dislocation centre located in site labelled [B]. We performed NEB calculations to compute the MEP between two first neighbours stable core configurations. According to the *Pbnm* space group symetry, these NEB calculations are thus designed to investigate the path between two different variants of the compact {021} core (*i.e,* between a [B] site of compact (021) core and a neighbour site of compact $(0\bar{2}1)$ core quoted [B']). Such calculations have been performed at various high pressures (between 4 and 10 GPa) and the resulting MEP are shown Figure 7. The paths are found to be asymmetric. According to an analysis of the atomic configurations, one can decompose the MEP into two elementary step. A first part of the path corresponds to a small displacement of the dislocation core in (001). In the second part, the dislocation is continuously shifted in a {021} plane corresponding to the spreading plane of the final configuration. Thus, in between, the core undergoes a modification to an activated core state configuration encountered for the rearrangement of the spreading between the two variants. In the pressure range 4–10 GPa, the activated state energy evolves from 1.3 eV/b to 2 eV/b (Table 4).

4. Discussion

Depending on the nature of the material, the effect of pressure on crystal strength may results from different effects on dislocations. Pressure may affect dislocation stability, dislocation mobility or the dislocation core structure itself [40,41]. In the case of forsterite, our systematic investigation of dislocation

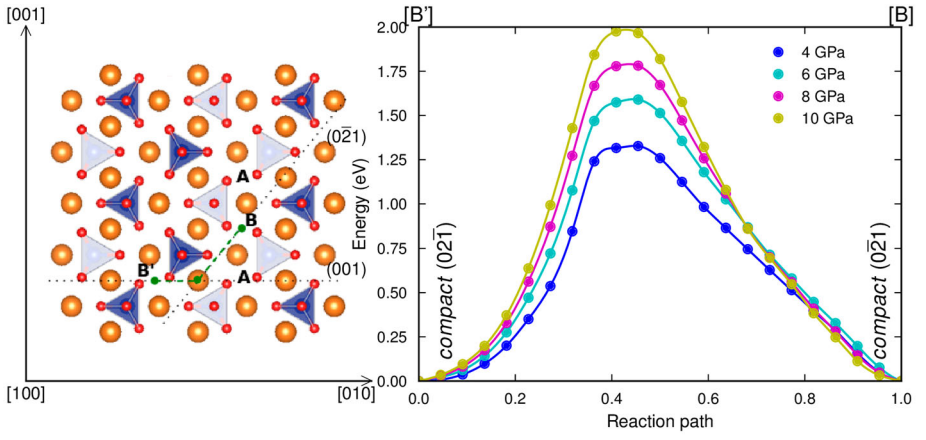

Figure 7. MEP between two compact {021} core variants computed for different high pressures (from 4 GPa to 10 GPa). Although, the two core variants are within {011}, the analysis of the core configurations along the path shows that the dislocation moves in (001) and {021} planes according to the green dotted path shown on the left side. The maximum of the MEP corresponds to an activated state with a dislocation located at the intersection between (001) and (02$\bar{1}$). The energies are given for a dislocation line of length b.

core structures with increasing pressure shows that [100] dislocation cores evolve from a spreading in (010) to one in {021}. Even at low pressure, a slight change of isostatic pressure can influence the atomic arrangement with a stable core which evolves from a split configuration to a compact one. This results from the dilatation state of [100] dislocation adopting a split (010) configuration. Indeed, as shown in Ref. [27], the dissociated state of the core into two collinear partials dislocations in (010) results in a strong positive strain tensor trace within the (010) spreading plane. This has two contributions, one from the staking fault and in a smaller extent the core of the two partials. As already mentioned in Ref. [27], the repulsion of ions apart the stacking plane associated with 1/2[100](010) has been initially measured in Ref. [42] with first principles calculations showing that such a dilation is not an artifact of the empirical potential. As pressure increases, the dissociation into 1/2[100] becomes consequently unfavourable. Pressure working against such a dilatation state of the dislocation core, at high pressure, the ground state configuration of

Table 4. Energy barrier (eV/b) associated with the transition between two compact {021} core configuration.

Pressure (GPa)	Max. energy (eV/b)	σ_c (GPa)
4	1.33	8.7–3.3
6	1.59	9.3–4.1
8	1.78	10.1–5.1
10	1.97	10.9–6.2

Note: As for Table 2, by using the dislocation core position projected in {011}, one can compute the stress required to overcome the MEP. Here, as the MEP is non-symetric, we report the two highest slopes associated with the displacement of the core in (010) and (021). Whatever the pressure, the maximum stress value is associated with the displacement of the dislocation core in (001).

the [100] screw dislocation adopts a compact {021} configuration. The relative stability of the different core configurations have therefore strong implications on the nature of the slip systems.

4.1. [100](010) slip system

Below 4 GPa, as the ground state configuration of the [100] screw dislocation corresponds to a spreading in (010), a [100](010) primary slip system can be expected. This is in agreement with the occurrence of this slip system reported in experiments at low pressure and high temperature [7,9,11,43,44]. The corresponding MEP, if plotted versus a reaction coordinate corresponding to the dislocation position along the path, reflects the Peierls potential V_P for glide in (010). Once the dislocation position is used to define V_P, critical stresses taken as the derivative of V_P can be calculated (Table 2). As the MEP in (010) are non monotonic, it seems reasonable to select the highest critical stress as a proxy for the Peierls stress. Nevertheless, this assumption can be further verified by performing NEB calculations with the application of simple shear strain component in order to promote glide in (010). A typical evolution of the minimum energy path as a function of applied stress σ_{xy} is shown Figure 8(a). From this kind of calculations, one can easily extract the evolution of the maximum slope of the Peierls potential and plot its evolution as a function of applied stress (Figure 8b). For the three low pressure conditions considered here, we find a good linear scaling of the maximum slope of V_P with respect to the applied stress suggesting that [100](010) Peierls potentials are rather insensitive to the applied stress. Thus, the highest critical stresses computed

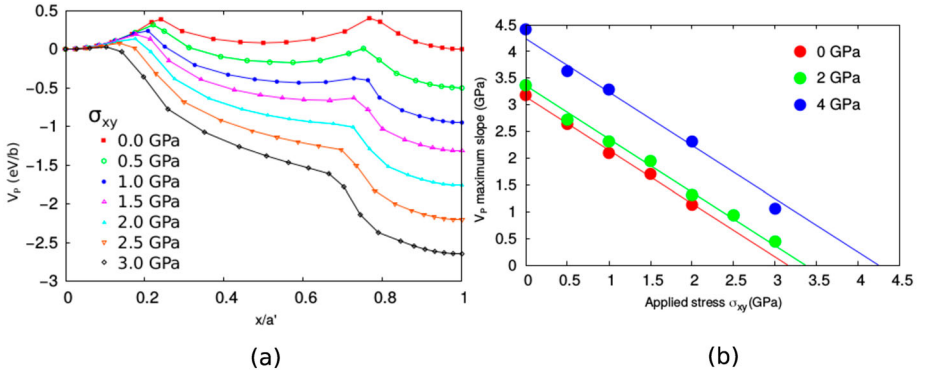

Figure 8. (a) Typical evolution of the Peierls potential V_P for [100](010) slip system with respect to an applied resolved shear stress. Here, the MEP depicting the Peierls potential is plotted versus the dislocation core position rescaled to the periodicity a' of the potential. (calculations performed for a pressure of 2 GPa). (b) Maximum slope of the Peierls potential V_P for [100](010) slip system versus the constant shear stress applied during a NEB calculation. As indicating by the linear dependency of the maximum slope with respect to the applied shear stress, the Peierls potential for [100](010) screw dislocation at low pressure is found stress independent.

from the free-stress Peierls potentials (Table 2) correspond to the Peierls stresses for [100](010) screw dislocations and evolve from 3.2 GPa at 0 GPa of pressure to 4.3 GPa for an isostatic pressure of 4 GPa. Above 4 GPa, as the ground state core configuration is mostly spread in {021}, [100](010) cannot be considered as a primary slip system.

4.2. [100]{011} slip systems

At high pressure above 4 GPa, the primary slip system of forsterite is then intrinsically related to the compact {021} core configuration. According to the stable core position in the crystal lattice and its core spreading, the nearest neighbours position of the dislocation at high pressure are aligned in {011} planes. In such planes, the dislocation occupies successively sites of alternative variants (denoted [B] and [B'] in Figure 7 and Figure 9). Thus, one may expect that the previous MEP (Figure 7) is involved in the glide of such compact {021} core in {011}. Indeed, as shown Figure 9 (with the reaction coordinate defined as the projection of dislocation core centres along the path), the full MEP for [100]{011}, computed between two identical core configurations, is composed of two mirrored MEP between [B] and [B'] sites. As for [100](010), estimates of the corresponding Peierls stress in {011} can be computed as the maximum derivative of the MEP with respect to the projected dislocation positions in the glide planes. For [100]{011} slip system between 4 and 10 GPa of pressure, the Peierls stresses would thus increase from 8.7 to 10.9 GPa (Table 4).

However, the glide of a screw dislocation in {011} is very peculiar as it is achieved through frequent flip between the two variants of the compact {021} core (Figure 9). The efficiency for the high pressure core to glide in {011} is then closely related to the capability of the dislocation to change its spreading plane from (021) to $(0\bar{2}1)$ and so-forth. Glide of screw dislocation involving complex path and frequent flip of the core is not restricted to the case of olivine. In *hcp* zirconium for instance, a similar feature has been reported for slip in the basal plane [45].

According to Figure 7 and its description in the previous section, the flipping of the compact {021} core configuration involves here two elementary events and a high energy activated state: on one hand, the highest slope of the MEP corresponds to a small displacement of the dislocation core in (001) and on the other hand, the slowest slope is the signature of the displacement of the core in a {021} plane. For all investigated pressures, the event corresponding to a small displacement of the core in (001) involves the critical stress (Table 4) which is the highest along the path, meaning that the slip in {011} should be triggered by a resolved shear stress in (001), i.e σ_{xz} with the convention adopted in this study. Therefore, for the highest pressure investigated here, we also computed the evolution of the MEP in {011} as a function of an applied stress σ_{xz} (Figure 10a). Despite the fact that at low σ_{xz} applied stress, the critical stress deduced

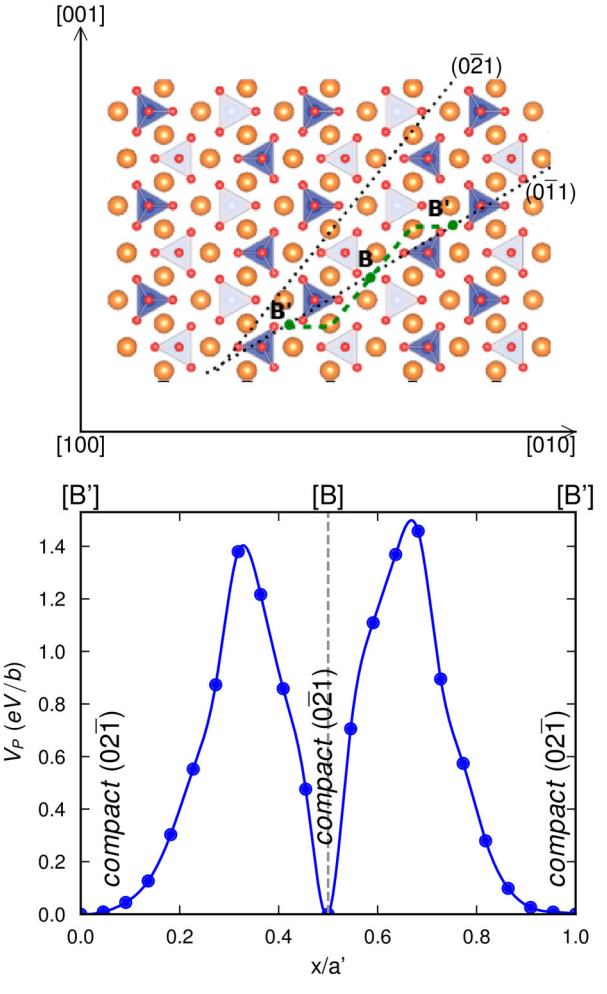

Figure 9. Peierls potential V_P for the glide of a straight screw dislocation line (length b) of Burgers vector [100] in {011} at high pressure (calculation performed at 6 GPa). Initial and final configurations are here strictly identical located in two successive [B′] sites distant from a length a' according to the green path sketched on the crystal structure. V_P is plotted as a function of the dislocation core position projected in {011}. As the dislocation moves from sites [B] to [B′], and [B′] to [B], the energy landscape is mirrored.

from the MEP scales with σ_{xz} (Figure 10b), for an applied σ_{xz} exceeding 5 GPa, the value of the energy barrier along the MEP vanishes suggesting that the activated state is sensitive to stress. As a consequence, stresses reported in Table 4 provide an upper bound limit for the Peierls stress for [100]{011} slip systems.

4.3. Pencil glide in (0kl)

As depicted by the green path drawn Figure 9, the compact {021} core is expected to glide in a zig-zag fashion around {011}. Moreover, as illustrated

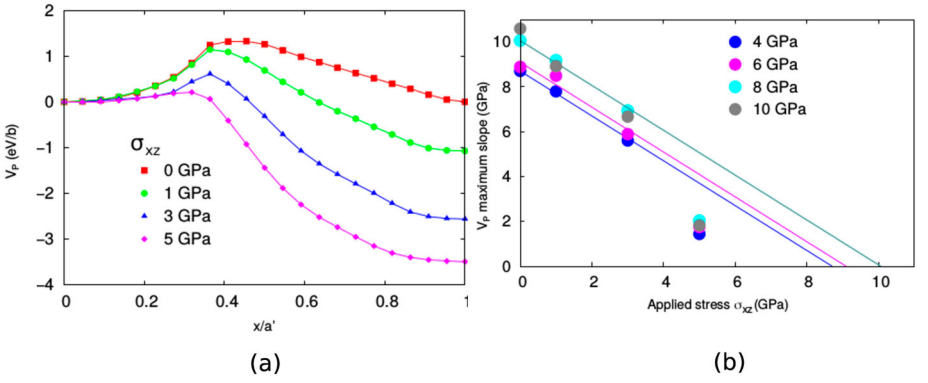

Figure 10. (a) Typical evolution of half of the Peierls potential for [100]{011} with respect to a shear stress resolved in (001). As for Figure 9, the calculations are done at 6 GPa of pressure and the potential is plotted with respect to the dislocation position projected in {011} between the sites [B] and [B′]. (b) Maximum slope of V_P for [100]{011} slip system versus a constant shear stress resolved in (001). The linearity breakdown highlights the sensitivity of the activated state to an applied σ_{xz} stress.

in Figure 10(b), the various core configurations involved in such glide seems to be strongly sensitive to the local stress state. Therefore, one cannot exclude various combinations of glide in {021} planes leading to define an average glide plane in any (0*kl*) even not crystallographic (Figure 11). From a purely mechanical point of view, such pencil glide, resulting from any combination of elementary glide of the compact {021} core between its variants, can be achieved provided the component of the stress σ_{xz} overcomes the maximum value found along the MEP (Figure 9). Thus, {011} is simply one among the available (0*kl*) glide planes but there is no reason to consider [100]{011} as a preferential slip system.

At low pressure, the stable core configuration is spread in (010), leading to a well-defined primary slip system [100](010). With such configuration, contrary

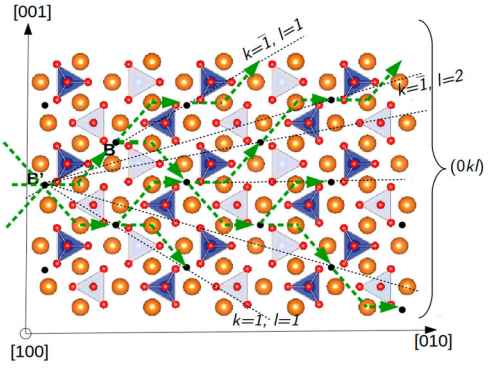

Figure 11. Illustration of pencil glide possibilities resulting from successive compact {021} core flipping.

to high pressure, the pencil glide is unexpected. However, there are experimental evidences that pencil glide is activated in olivine at low pressure [4]. For this to occur, the dislocation core spread in (010) must transform into the compact {021} core configuration. Such a transition can be viewed as a cross-slip. However, unlike classical cross-slip reported in *fcc* or *bcc* metals, here the parent and cross-slipped cores differ not only by the orientation of the glide plane but also by the core structures. This specific cross-slip event requires to overcome the energy barrier depicted in Figure 6. Below 4 GPa, the cross-slip energy is around 1 eV/b. These energies are higher than the barrier involved in the glide in (010) but close to the ones for glide in (0*kl*) (as shown for instance by our calculations performed at 4 GPa of isostatic pressure). Thus, it can be expected than the low pressure dislocation core can cross-slip into a compact {021} core glissile in (0*kl*) according to the mechanism discussed above. It is worth mentioning that experimental evidences of cross-slip for [100] dislocations have been reported. Indeed, Raterron and coworkers reported the occurrence of cross-slip of [100] dislocations in deformed samples exhibiting [100] dislocation loops in gliding configuration in (010) [46,47]. Nevertheless, as cross-slip is known to be sensitive to the stress state, including non-glide stress effects, a detailed study of the cross-slip of [100] screw dislocation will be required. Such an extended study should be performed on finite dislocation length simulation which is out of the scope of the present work based on infinite straight dislocation. Indeed, if cross-slip in olivine follows the dominant Friedel–Escaig mechanism documented in *fcc* metals, the mechanism will involve local constriction of the dislocation core in the initial (010) glide plane followed by a spreading in the {021} cross-slip plane.

5. Conclusion

Based on atomistic simulations of dislocation core structures, we demonstrate the existence of several screw dislocation core configurations for [100] dislocation in olivine.

- At low pressure, the core of the dislocations is spread in (010) leading to a primary [100](010) slip system.
- At higher pressure (i.e. greater than 4 GPa), spreading in (010) is unfavourable and [100](010) cannot be considered as a primary slip system.
- The dislocation core can spread in two equivalent {021} planes. This can lead to a diversity of glide paths with in average at a macroscopic scale glide in any {0*kl*} planes.

Our analysis of the dislocation core structures thus provides the first interpretation of pencil glide of [100] dislocations in olivine. This tendency for pencil glide appears to be stronger at high pressure.

Disclosure statement

No potential conflict of interest was reported by the authors.

Funding

This work was supported by funding from the European Research Council under the Seventh Framework Programme (FP7), ERC Grant No 290424 - RheoMan. Computational resources were provided by the CRI-Université de Lille.

ORCID

Ph. Carrez http://orcid.org/0000-0003-1295-9377
P. Cordier http://orcid.org/0000-0002-1883-2994

References

[1] G.I. Taylor and C.F. Elam, *The distortion of iron crystals*. Proc. R. Soc. A: Math. Phys. Eng. Sci. 112 (1926), pp. 337–361.
[2] A.H.W. Ngan, *A generalized Peierls-Nabarro model for nonplanar screw dislocation cores*. J. Mech. Phys. Solids 45 (1997), pp. 903–921.
[3] A.H.W. Ngan, *A new model for dislocation kink-pair activation at low temperatures based on the Peierls-Nabarro concept*. Philos. Mag. A 79 (1999), pp. 1697–1720.
[4] C.B. Raleigh, *Mechanisms of plastic deformation of olivine*. J. Geophys. Res. 73 (1968), pp. 5391–5406.
[5] D.L. Kohlstedt, C. Goetze, W.B. Durham and J.V. Sande, *New technique for decorating dislocations in olivine*. Science 191 (1976), pp. 1045–1046.
[6] Y. Gueguen, *Dislocations in naturally deformed terrestrial olivine: classification, interpretation, applications*. Bull. Mineral 102 (1979), pp. 178–183.
[7] W.B. Durham and C. Goetze, *Plastic flow of oriented single crystals of olivine: 1. mechanical data*. J. Geophys. Res. 82 (1977), pp. 5737–5753.
[8] B. Evans and C. Goetze, *The temperature variation of hardness of olivine and its implication for polycrystalline yield stress*. J. Geophys. Res. 84 (1979), pp. 5505–5524.
[9] M. Darot and Y. Gueguen, *High-temperature creep of forsterite single crystals*. J. Geophys. Res.: Solid Earth 86 (1981), pp. 6219–6234.
[10] R.J. Gaboriaud, M. Darot, Y. Gueguen and J. Woirgard, *Dislocations in olivine indented at low temperatures*. Phys. Chem. Miner. 7 (1981), pp. 100–104.
[11] S.J. Mackwell, D.L. Kohlstedt and M.S. Paterson, *The role of water in the deformation of olivine single crystals*. J. Geophys. Res.: Solid Earth 90 (1985), pp. 11319–11333.
[12] Y. Wang, R.C. Liebermann and J.N. Boland, *Olivine as an in situ piezometer in high pressure apparatus*. Phys. Chem. Miner. 15 (1988), pp. 493–497.
[13] M. Panning and B. Romanowicz, *Inferences on flow at the base of Earth's mantle based on seismic anisotropy*. Science 303 (2004), pp. 351–353.
[14] J. Durinck, P. Carrez and P. Cordier, *Application of the Peierls-Nabarro model to dislocations in forsterite*. Eur. J. Mineral. 19 (2007), pp. 631–639.
[15] P. Carrez, A. Walker, A. Metsue and P. Cordier, *Evidence from numerical modelling for 3D spreading of [001] screw dislocations in Mg_2SiO_4 forsterite*. Philos. Mag. 88 (2008), pp. 2477–2485.

[16] D. Mainprice, A. Tommasi, H. Couvy, P. Cordier and D.J. Frost, *Pressure sensitivity of olivine slip systems and seismic anisotropy of Earth's upper mantle*. Nature 433 (2005), pp. 731–733.
[17] H. Jung, I. Katayama, Z. Jiang, T. Hiraga and S. Karato, *Effect of water and stress on the lattice-preferred orientation of olivine*. Tectonophysics 421 (2006), pp. 1–22.
[18] V. Bulatov and W. Cai (eds.), *Computer Simulations of Dislocations*, Oxford University Press, Oxford, 2006.
[19] C.R.A. Catlow, *Point defect and electronic properties of uranium dioxide*. Proc. R. Soc. Lond. A 353 (1977), pp. 533–561.
[20] G.V. Lewis and C.R.A. Catlow, *Potential models for ionic oxides*. J. Phys. C: Solid State Phys 18 (1985), pp. 1149–1161.
[21] G.D. Price, S.C. Parker and M. Leslie, *The lattice dynamics of forsterite*. Mineral. Mag. 51 (1987), pp. 157–170.
[22] M.J. Sanders, M. Leslie and C.R.A. Catlow, *Interatomic potentials for SiO_2,*. J. Chem. Soc., Chem. Commun 0 (1984), pp. 1271–1273.
[23] B.G. Dick and A.W. Overhauser, *Theory of the dielectric constants of alkali halide crystals*. Phys. Rev. 112 (1958), pp. 90–103.
[24] C.R.A. Catlow and G.D. Price, *Computer modelling of solid-state inorganic materials*. Nature 347 (1990), pp. 243–248.
[25] N.C. Richmond and J.P. Brodholt, *Incorporation of Fe^{3+} into forsterite and wadsleyite*. Am. Mineral. 85 (2000), pp. 1155–1158.
[26] A.M. Walker, J.D. Gale, B. Slater and K. Wright, *Atomic scale modelling of the cores of dislocations in complex materials part 2: applications*. Phys. Chem. Chem. Phys 7 (2005), pp. 3235–3242.
[27] S. Mahendran, P. Carrez, S. Groh and P. Cordier, *Dislocation modelling in Mg_2SiO_4 forsterite: an atomic-scale study based on the THB1 potential*. Modell. Simul. Mater. Sci. Eng. 25 (2017), pp. 054002.
[28] R. Skelton and A.M. Walker, *Lubrication of dislocation glide in forsterite by Mg vacancies: Insights from Peierls-Nabarro modeling*. Phys. Earth Planet. Inter. 287 (2019), pp. 1–9.
[29] G.D. Price, S.C. Parker and M. Leslie, *The lattice dynamics and thermodynamics of the Mg2SiO4 polymorphs*. Phys. Chem. Miner. 15 (1987), pp. 181–190.
[30] B. Reynard, G.D. Price and P. Gillet, *Thermodynamic and anharmonic properties of forsterite, a-Mg_2SiO_4: computer modelling versus high-pressure and high-temperature Measurements*. J. Geophys. Res.: Solid Earth 97 (1992), pp. 19791–19801.
[31] S. Plimpton, *Fast parallel algorithms for short-range molecular dynamics*. J. Comput. Phys. 117 (1995), pp. 1–19.
[32] G. Henkelman, B.P. Uberuaga and H. Jonsson, *A climbing image nudged elastic band method for finding saddle points and minimum energy paths*. J. Chem. Phys. 113 (2000), pp. 9901–9904.
[33] P.J. Mitchell and D. Fincham, *Shell model simulations by adiabatic dynamics*. J. Phys.: Condens. Matter 5 (1993), pp. 1031–1038.
[34] N.H. de Leeuw and S.C. Parker, *Molecular-dynamics simulation of MgO surfaces in liquid water using a shell-model potential for water*. Phys. Rev. B 58 (1998), pp. 13901–13908.
[35] X. Sun, Y. Chu, T. Song, Z. Liu, L. Zhang, X. Wang, Y. Liu and Q. Chen, *Application of a shell model in molecular dynamics simulation to ZnO with zinc-blende cubic structure*. Solid State Commun. 142 (2007), pp. 15–19.

[36] Y. Zhang, J. Hong, B. Liu and D. Fang, *Molecular dynamics investigations on the size-dependent ferroelectric behavior of $BaTiO_3$ nanowires*. Nanotechnology 20 (2009), pp. 405703.
[37] W. Cai, *Modeling dislocations using a periodic cell*, in *Handbook of Materials Modeling*, Springer, Dordrecht, 2005. pp. 813–826.
[38] N. Lehto and S. Öberg, *Effects of dislocation interactions: application to the period-doubled core of the 90° partial in silicon*. Phys. Rev. Lett 80 (1998), pp. 5568–5571.
[39] S. Ismail-Beigi and T.A. Arias, *Ab initio study of screw dislocations in Mo and Ta: a new picture of plasticity in bcc transition metals*. Phys. Rev. Lett 84 (2000), pp. 1499–1502.
[40] P. Hirel, A. Kraych, P. Carrez and P. Cordier, *Atomic core structure and mobility of [100](010) and [010](100) dislocations in $MgSiO_3$ perovskite*. Acta Mater. 79 (2014), pp. 117–125.
[41] P. Carrez, J. Godet and P. Cordier, *Atomistic simulations of 1/2 < 110 > screw dislocation core in magnesium oxide*. Comput. Mater. Sci. 103 (2015), pp. 250–255.
[42] J. Durinck, A. Legris and P. Cordier, *Pressure sensitivity of olivine slip systems: first-principle calculations of generalised stacking faults*. Phys. Chem. Miner. 32 (2005), pp. 646–654.
[43] P. Phakey, G. Dollinger, and J. Christie, *Transmission electron microscopy of experimentally deformed olivine crystals*, in *Flow and Fracture of Rocks*, Vol. 16, American Geophysical Union Monograph Series, Washington, D. C., 1972, pp. 117–138.
[44] D.L. Kohlstedt and C. Goetze, *Low-stress, high- temperature creep in olivine single crystals*. J. Geophys. Res. 79 (1974), pp. 2045–2051.
[45] N. Chaari, E. Clouet and D. Rodney, *First-principles study of secondary slip in zirconium*. Phys. Rev. Lett 112 (2014), pp. 075504.
[46] P. Raterron, J. Chen, L. Li and P. Cordier, *Pressure-induced slip-system transition in forsterite: single-crystal rheological properties at mantle pressure and temperature*. Am. Mineral. 92 (2007), pp. 1436–1445.
[47] L. Li, D. Weidner, P. Raterron, J. Chen, M. Vaughan, S. Mei and B. Durham, *Deformation of olivine at mantle pressure using the D-DIA*. Eur. J. Mineral. 18 (2006), pp. 7–19.